

Wavescan: multiresolution regression of gravitational-wave data

S. Klimenko¹

¹ *University of Florida, P.O.Box 118440, Gainesville, Florida, 32611, USA*

Identification of a transient gravitational-wave signal embedded into non-stationary noise requires the analysis of time-dependent spectral components in the resulting time series. The time-frequency distribution of the signal power can be estimated with Gabor atoms, or wavelets, localized in time and frequency by a window function. Such analysis is limited by the Heisenberg–Gabor uncertainty, which does not allow a high-resolution localization of power with individual wavelets simultaneously in time and frequency. As a result, the temporal and spectral leakage affects the time-frequency distribution, limiting the identification of sharp features in the power spectrum. This paper presents a time-frequency regression method where instead of a single window, a stack of wavelets with different windows spanning a wide range of resolutions is used to scan power at each time-frequency location. Such a wavelet scan (dubbed in the paper as wavescan) extends the conventional multiresolution analysis to capture transient signals and remove the local power variations due to the temporal and spectral leakage. A wavelet, least affected by the leakage, is selected from the stack at each time-frequency location to obtain the high-resolution localization of power. The paper presents all stages of the multiresolution wavescan regression, including the estimation of the time-varying spectrum, identification of transient signals in the time-frequency domain, and reconstruction of the corresponding time-domain waveforms. To demonstrate the performance of the method, the wavescan regression is applied to the gravitational wave data from the LIGO detectors.

I. INTRODUCTION

Analysis of time series with time-dependent spectral density is a challenging problem in signal processing. Often signals present in noisy data may have rapidly varying temporal and spectral components with a sharp localization of the signal power in time and frequency. To obtain the time-frequency representation of the time series $x(t)$, the most widely-used is the short-time (window) Fourier transform (STFT) [1]

$$X(\tau, \omega) = \int_{-\infty}^{\infty} x(t)w(t - \tau)e^{-i\omega t} dt, \quad (1)$$

where the analysis window $w(t - \tau)$ of a finite duration captures the signal power centred around time τ and frequency ω . The time-frequency distribution (or spectrogram) is estimated as $P(\tau, \omega) = |X(\tau, \omega)|^2$. The window function w determines the STFT resolutions in time (effective duration δt) and frequency (effective bandwidth $\delta \omega$) constrained by the Heisenberg–Gabor uncertainty $\delta t \delta \omega \geq 1/2$ [2]. In general, it is not possible to optimally describe all temporal and spectral components in the data by selecting a single window. For example, a gravitational wave (GW) signal from a collision of two black holes [3], with the amplitude and frequency increasing with time (so-called chirp), requires the time resolution of $\delta t \geq 1$ s at the early stage of the binary evolution and $\delta t \leq 0.01$ s at the end of the binary evolution when the system merges. For chirping GW signals, this limitation can be partially alleviated by using the conventional wavelet transforms [4], where the wavelet basis is obtained by scaling a single mother wavelet and all wavelets have the same number of cycles. As a result, the wavelet duration decreases as its frequency increases, improving the estimation of the GW power at the merger stage. Such multiresolution wavelets are widely

used for the time-frequency visualization of detected GW signals [5, 6]. However, they require individual tuning of the transform parameters for each GW chirp, and for many transient signals, the conventional wavelet representation could be quite sub-optimal.

To overcome the trade-off between the time and frequency resolution and improve the time-frequency localization of the temporal and spectral components, different high-resolution techniques have been proposed [7], starting with the Wigner-Ville (WV) transform [8, 9]. The WV distribution provides the best possible time-frequency localization, but it suffers from the cross-term artifacts for multi-component signals. The WV artifacts can be partially suppressed by introducing smoothing kernels resulting in a variety of time-frequency distributions $P(\tau, \omega)$ [10], which usually satisfy the marginals: e.g. $\int P(\tau, \omega) d\omega = x^2(\tau)$ and $\int P(\tau, \omega) d\tau = |S(\omega)|^2$, where $S(\omega)$ is the Fourier transform of $x(t)$. A different approach to the high-resolution techniques is based on the multiple STFT spectrograms obtained with different time-frequency resolutions that are combined together into a single spectrogram [11–13]. Such spectrograms improve the visualization of the time-frequency data, but still, they are affected by the artifacts due to the temporal and spectral leakage, and usually, they do not satisfy the marginals.

All the high-resolution techniques mentioned above aim to identify a joint time-frequency distribution (TFD) that would satisfy our intuitive expectations of a time-varying spectrum. TFDs provide a valuable tool in the time-frequency analysis helping us to identify and characterize transient signals, particularly when their characteristic waveforms are not known a priori and the construction of the matched filters is not possible. Most likely, TFDs should be constructed separately for different situations and may have a different interpretation for the

stochastic noise and deterministic signals. Also, TFDs alone are not sufficient to perform signal filtering and synthesis. For example, to identify and extract a GW signal [14], the time series from several detectors should be mapped into the time-frequency domain, preserving the polarization state and the complex structure of the signal. This multi-dimensional data should be filtered to extract the GW signal, and its time-domain waveforms should be reconstructed.

Such model-agnostic analysis, filtering, and synthesis of gravitational waves had been implemented in the GW data analysis pipeline called WaveBurst [14–17]. For the TFD estimation, it uses the orthonormal Wilson-Daubechies-Meyer (WDM) transform [18], where the basis functions are constructed to have the same resolution across the frequency scale. Similar to the STFT and the traditional wavelets, the WDM transform at a fixed resolution is not capable of efficiently capturing a multi-component signal. To improve the identification of such signals, the WDM transform is performed at several (typically 7-8) resolutions, producing an oversampled TF representation of data. The WDM amplitudes from all resolutions are analyzed together to identify and reconstruct GW signals in the WDM domain [14]. The time-domain GW waveforms can be also reconstructed by using the inverse WDM transform.

The WDM technique had been successfully used for the first direct observation of gravitational waves from the merger of two black holes [19], and for detection of gravitational wave signals [20–22] in the data collected by the advanced LIGO and Virgo detectors [23, 24]. However, despite its multiresolution approach, the WDM transform is affected by the temporal and spectral leakage hindering the efficient identification of GW signals in the time-frequency data.

The goal of this work is to obtain the leakage-free time-frequency distribution. It is based on the multiple STFTs where the optimal resolution at each time-frequency location is dynamically selected according to the wavescan algorithm. The resulting wavescan transform can be used for the model-agnostic analysis, filtering, and synthesis of gravitational-wave signals.

The rest of the paper is organized as follows. Section II introduces the wavescan method, including the description of the wavescan transform and the definition of the high-resolution time-frequency distribution. Section III introduces the excess power and the cross-power statistics used to identify signals in the time-frequency data. Section IV discusses the reconstruction of the time-domain signals from the time-frequency data, e.g. the inverse wavescan transform, followed by the conclusion.

II. WAVESCAN

The wavescan method utilizes multiple STFTs with the analysis windows of different duration. For a given TF location $\tau = t_n$ and $\omega = \omega_m$, and the analysis window

w_l , Equation 1 defines the two wavelet amplitudes X_{lnm} and \tilde{X}_{lnm} given by the inner product

$$\langle x, \phi \rangle = \int x(t) \phi(t) dt, \quad (2)$$

of $x(t)$ with the symmetric $\phi = \psi_{lnm}$ and anti-symmetric $\phi = \tilde{\psi}_{lnm}$ atomic Gabor waveforms referred below as (STFT) wavelets

$$\psi_{lnm}(t) = w_l(t - t_n) \cos[\omega_m(t - t_n)], \quad (3)$$

$$\tilde{\psi}_{lnm}(t) = w_l(t - t_n) \sin[\omega_m(t - t_n)]. \quad (4)$$

The STFT wavelets organised in stacks where the wavelets with different resolution l are centered at the same time t_n and frequency ω_m . The wavelet stacks are constructed by scaling the duration of the window function w_l : $T_w[l] = \alpha^{l-1} T_o$, $1 \leq l \leq L$, where T_o is the duration of the shortest window, L is the total number of resolutions in the stack, and $1 < \alpha \leq 2$ is the scaling parameter. Each window function is normalized to the unity norm. The window can be selected to have the Gaussian shape, which is optimally localized with $\delta t \delta \omega = 1/2$. However, the Gaussian window is not localized in time, and in general, other close to optimal window functions with compact support can be considered. Specifically, in this study, the Blackmanharris window is used.

The wavescan stacks form a regular sampling lattice

$$t_n = n \Delta t, \quad \omega_m = m \Delta \omega, \quad (5)$$

where Δt and $\Delta \omega$ are the sampling steps in time and frequency. The wavescan lattice is highly oversampled with $\Delta t \leq \delta t_{min}$ and $\Delta f \leq \delta f_{min}$, where δt_{min} is the effective duration of the shortest wavelet and $\delta \omega_{min}$ is the effective bandwidth of the longest wavelet in the stack.

The power P_{lnm} (or amplitude A_{lnm}) of the wavescan data is defined as

$$P_{lnm} = \frac{1}{2} [a_{lnm}^2 + \tilde{a}_{lnm}^2], \quad A_{lnm} = \sqrt{P_{lnm}}, \quad (6)$$

$$a_{lnm} = \frac{X_{lnm}}{|\psi_{lnm}|}, \quad \tilde{a}_{lnm} = \frac{\tilde{X}_{lnm}}{|\tilde{\psi}_{lnm}|}, \quad (7)$$

where the STFT amplitudes are normalized by the norm ($|\phi| = \sqrt{\langle \phi, \phi \rangle}$) of the corresponding wavelet function.

To illustrate the problem with the temporal and spectral leakage, the following test data is used, including the four different simulated signals: a) a monochromatic line, b) a linear chirp, c) a broadband cos-Gaussian burst with the duration of 0.016 seconds and d) a GW chirp. All these signals are injected into a white Gaussian noise with the unity variance. The parameters of the Gabor transform are: $T_o = 1/64$ s, $L = 8$, $\alpha = 2$, $\Delta t = 1/256$ s, $\Delta \omega / 2\pi = 2$ Hz. Figure 1 shows the TFD estimator $A_{max}(t_n, \omega_m) = \max_l(A_{lnm})$, which may look like a natural choice for identification of weak signals in the noisy data. However, the A_{max} TFD demonstrates a clear problem: both the deterministic signals and the noise

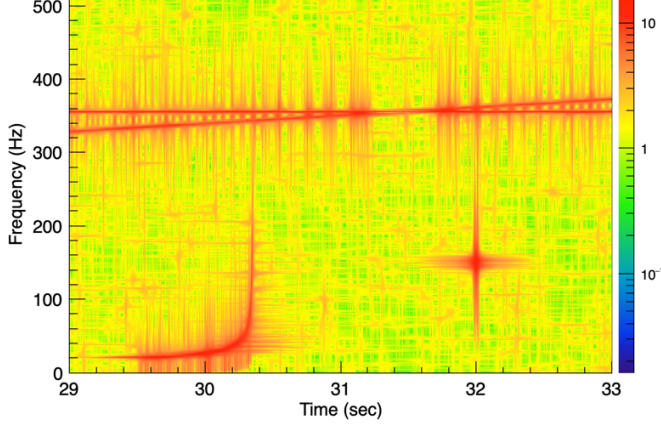


FIG. 1. Time-frequency distribution obtained with the A_{max} estimator, which is affected by the temporal and spectral leakage.

show severe artifacts due to the temporal and spectral leakage.

In wavescan the TFD artifacts are suppressed by selecting a wavelet in each stack that is less affected by the leakage. The identification of the optimal wavelet is different for the stochastic noise and deterministic signals. Let us focus on the noise first. By using the overlap between the wavescan wavelets

$$O_{ij} = \frac{\langle \psi_{inm}, \psi_{jnm} \rangle}{|\psi_{inm}| |\psi_{jnm}|}, \quad \tilde{O}_{ij} = \frac{\langle \tilde{\psi}_{inm}, \tilde{\psi}_{jnm} \rangle}{|\tilde{\psi}_{inm}| |\tilde{\psi}_{jnm}|}. \quad (8)$$

the cross-talk coefficient between the wavelet i and all other wavelets in the stack are defined as follows

$$C_i = \frac{1}{\sum_{j \neq i} A_i A_j} \sum_{j \neq i} (a_i a_j Q_{ij} + \tilde{a}_i \tilde{a}_j \tilde{Q}_{ij}). \quad (9)$$

The cross-talk coefficient C_i is a function of time and frequency, but to simplify the equations, the (n, m) dependence is omitted. Then the cross-talk statistics are defined as

$$\lambda_c = (C_{\max} + C_{\min}), \quad \lambda_p = (C_{P\max} + C_{P\min})/\sqrt{2}, \quad (10)$$

where C_{\max} and C_{\min} are the maximum and minimum values of C_i in the stack, and $C_{P\max}$ and $C_{P\min}$ are the cross-talk values corresponding to the maximum and minimum power in the stack. The purpose of the statistics λ_c and λ_p is to identify the local dips and bumps in the noise TFD. If $\lambda_c < \lambda_p$ or $\lambda_c < 0.5$, there is a local dip, and a wavelet with the cross-talk C_{\min} is selected. Otherwise, there is a local bump, and a wavelet with the cross-talk C_{\max} is selected. This condition suppresses most of the temporal and spectral leakage in the stochastic noise, but it is not highly effective for deterministic signals.

Because of the high overlap between the adjacent wavelets in a stack, one should not expect a large power drop between the resolutions unless the stack is affected by the leakage. This can be characterized by the maximum power drop in the stack defined as

$$F_d = \text{MAX}_l \left\{ \frac{|P_l - P_{l+1}|}{\text{MIN}(P_l, P_{l+1}) + \sigma^2} \right\}, \quad (11)$$

where the variance of the noise σ^2 is used to suppress the large F_d variations due to the noise fluctuations. Wavelet stacks with the large power drop $F_d > 2$ are affected by the leakage, and in this case a wavelet with the minimum power in the stack is selected. This condition removes the leakage induced by the deterministic signals. On the other hand, when a wavelet stack is not affected by the leakage, the stack amplitudes are expected to change in a predictable way $a_l \sim a_I O_{Il}$ and $\tilde{a}_l \sim \tilde{a}_I \tilde{O}_{Il}$, where (a_I, \tilde{a}_I) are the wavescan amplitudes corresponding to the maximum power in the stack, and (O_{Il}, \tilde{O}_{Il}) are the overlap coefficients between the wavelets l and I . Therefore, such wavelet stacks should have a low value of the power disbalance

$$D_p = \sqrt{2} \sum_l [(a_I O_{Il} - a_l)^2 + (\tilde{a}_I \tilde{O}_{Il} - \tilde{a}_l)^2 + 2\sigma^2]. \quad (12)$$

When a wavelet stack satisfies the condition $D_p < \lambda_p^2 P_I$, the wavelet with the maximum power P_I is selected. The power disbalance helps to recover the optimal resolution for deterministic signals that could be missed by the other conditions. The last two conditions on F_d and D_p do not affect the selection of the optimal wavelet for the stochastic noise with the variance σ^2 . We could always consider whitened data with the unit noise variance, e.g. $\sigma^2 = 1$.

Figure 2 shows that the proposed wavescan algorithm efficiently removes the leakage artifacts. Compared to the geometric mean (GM) estimator [13, 25], shown in the left panel of Figure 2, the wavescan demonstrates a better signal localization and much lower pollution of the TFD with the leakage artifacts. This is confirmed by the power spectral density distributions shown in Figure 3(left) in comparison with the reference spectrum obtained with the WDM transform. The wavescan and the WDM distributions are in a good agreement, while the GM distribution is affected by the leakage artifacts and underestimates the signal power. Figure 3 shows that the wavescan also correctly reproduces the test noise distribution obtained with the orthonormal WDM transform.

Because of its discrete selection of the optimal wavelet, wavescan may underestimate the noise power in the vicinity of the transient events (blue spots in the left panel of Figure 3). This is due to the selection of wavelets with the minimum power in the stack when the leakage conditions are identified. While these artifacts can be corrected, they are cosmetic, and do not obstruct the visualization, identification and reconstruction of transient events.

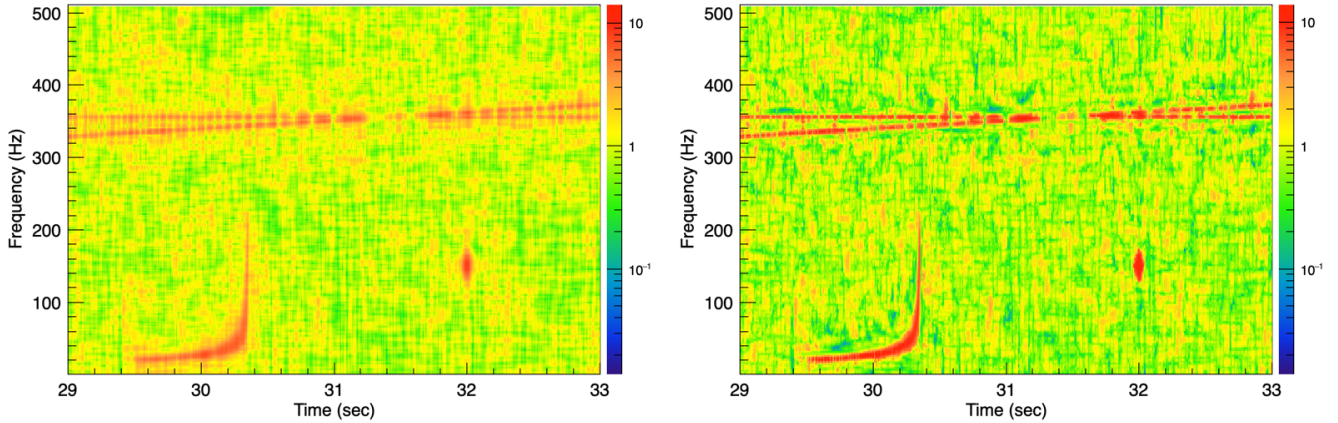


FIG. 2. Time-frequency distributions: left - geometric mean, right - wavescan.

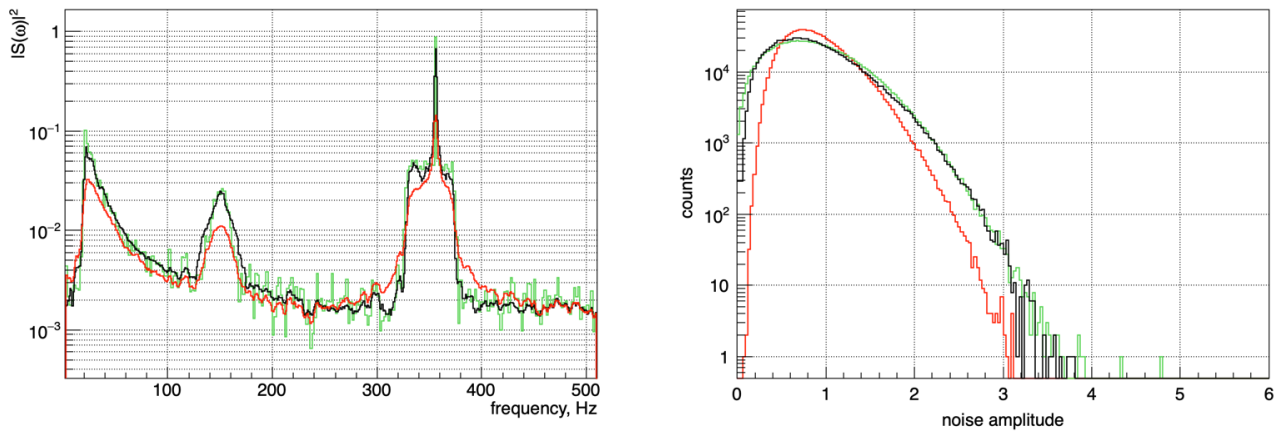


FIG. 3. Left panel: Power spectral density distribution $|S(\omega)|^2 = \int P(t, \omega) dt$ of the test data for the wavescan (black), GM (red) and WDM (green) estimators for the frequency binning of 2 Hz. Right panel: Comparison of the test noise distributions from the wavescan (black), from the GM (red) and from the orthonormal WDM transform (green).

The result of the wavescan transform is a high-resolution wavelet data where each sampled time-frequency location (or pixel) is described by the two wavelet amplitudes obtained by the convolution of the time-domain data with the corresponding STFT wavelets (Equations 3-4). The resolution of the STFT wavelets varies from pixel to pixel according to the wavescan algorithm. The wavescan transform suppresses artifacts due to the temporal and spectral leakage, and provide a high-resolution spectrograms of the time-varying power. As an example, Figure 4 displays the spectrograms of the first GW signal GW150914 detected by the LIGO Hanford and Livingston observatories in 2015 [19] clearly showing the chirping BBH signal in both detectors. The improved time-frequency localization and reduced leakage are particularly beneficial for the identification and reconstruction of GW signals discussed in the next two sections.

III. SIGNAL IDENTIFICATION

This section describes the identification of a weak gravitational wave signal in the non-stationary data from a network of GW detectors. After the data is conditioned to remove predictable spectral artifacts like quasi-monochromatic lines [26], the detector noise is approximated as a superposition of the quasi-stationary colored Gaussian noise and the transient noise artifacts (glitches) due to the environmental and instrumental disturbances [27]. The spectral amplitude density of the quasi-stationary noise $S_k(\omega)$ is estimated with the high-frequency resolution WDM transform [18]. The noise-scaled (whitened) time-series $x_k(t)$ for each detector $k = 1, 2, \dots, K$ in the network are obtained with the inverse WDM transform.

A search for a transient GW signal with the two polarisation $h_+(t)$ and $h_\times(t)$ is performed assuming that the

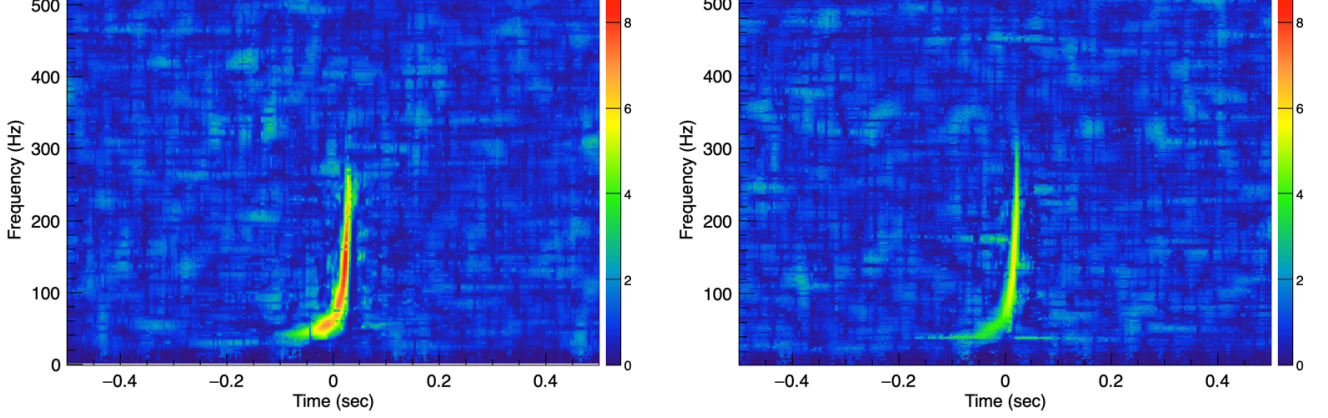


FIG. 4. Wavescan spectrograms for the first GW signal GW150914 detected by LIGO [19]: left-Hanford detector, right-Livingston detector.

characteristic signal waveforms ξ_k in each detector are not known a priori

$$\xi_k(t) = F_{+k}(\theta, \phi)h_{+k}(t) + F_{\times k}(\theta, \phi)h_{\times k}(t). \quad (13)$$

Where the detector antenna patterns F_{+k} and $F_{\times k}$ depend on the source location θ and ϕ in the sky and the detector orientation [14]. In this case the construction and use of the matched filters is not possible. Therefore, the analysis is performed in the wavescan domain by looking for transient signals with the amplitudes inconsistent with the fluctuations of the quasi-stationary detector noise. The corresponding wavescan amplitudes can be identified by using the excess-power and/or cross-power statistics described below.

Since the source location in the sky is not usually known, the network excess power defined for each pixel should be maximized over all possible time-of-flight delays τ_k of the anticipated signal

$$P_{net} = \sum_k r_k P_k(\tau_k), \quad r_k = (1/S_k) / (\sum_i 1/S_i). \quad (14)$$

This is obtained by calculating the time-delayed wavescan amplitudes for each detector. The weight coefficients r_k are accounting for the differences in the detector spectral sensitivities S_k .

The cross power between the two detectors i and j is calculated individually for each time-frequency pixel and defined as

$$C_{ij} = \frac{r_i r_j P_i^2 P_j^2}{(r_j P_i + r_i P_j)^2}. \quad (15)$$

Respectively, the network cross-power is defined as.

$$C_{net} = \sum_{i < j} R_{ij} C_{ij}, \quad R_{ij} = \frac{1/\sqrt{S_i S_j}}{\sum_{k < l} 1/\sqrt{S_k S_l}}. \quad (16)$$

To distinguish signals from noise, the cross-power statistic uses the coherent signature of the GW signals that produce near-simultaneous responses with consistent waveforms in different detectors.

The statistics P_{net} and C_{net} approximately follow the Gamma distribution, which parameters depend on the number of detectors used in the analysis and their relative sensitivities. To obtain a more universal, network-independent statistics, the following procedure is used. First, the distribution shape parameter κ is estimated using the maximum likelihood method [28]. The statistics P_{net} is normalized by the factor $\gamma \mu_p$, where μ_p is the mean of the P_{net} distribution. The parameter γ is given by the solution of the equation

$$\gamma = \gamma_o^{\frac{1}{2\kappa}} e^{-(1-\gamma)}, \quad \gamma_o = \frac{\kappa - 1}{\kappa}, \quad (17)$$

which defines the optimal mapping between the Gamma and the half-normal distributions. It can be solved by iterations with the initial $\gamma = \gamma_o$. Then, a new statistic a_p is calculated as

$$a_p^2 = 2\kappa \gamma^2 \frac{\gamma}{\gamma_o} \frac{\mu_p}{\nu_p} [(y - 1) - \log(y)], \quad y = \frac{P_{net}}{\gamma \mu_p}. \quad (18)$$

The statistic $a_p(y)$ is defined for $y > 1$ with the pixel power close to or above the median ν_p of the P_{net} distribution. Therefore, the noise pixels with the lowest amplitudes can be excluded from the analysis, and for $a_p > 0.5$ the remaining noise amplitudes closely follow the half-normal distribution with the unity variance. Following the same procedure, the corresponding statistic a_c can be also constructed for the C_{net} distribution.

Time-series from the gravitational-wave detectors are highly non-stationary, containing the noise transients due to the environmental and instrumental disturbances [27, 29]. Figure 5 shows the example of the a_p and a_c distributions for the real noise of the Livingston (L) and Hanford

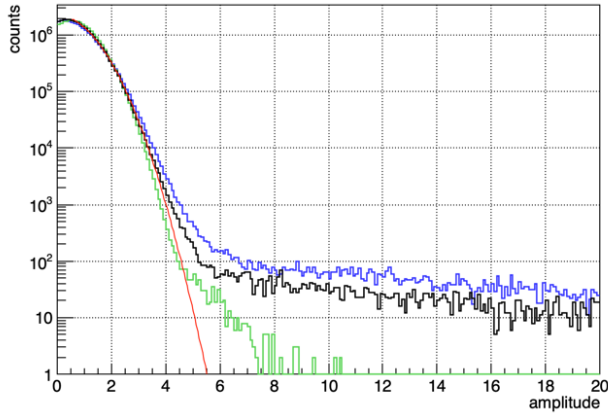


FIG. 5. The network-independent statistics for the Hanford-Livingston network noise: black - wavescan excess-power, green - wavescan cross-power, blue - geometric mean excess-power, red - half-normal distribution with the unity variance.

(H) detectors [23]. As expected, the excess-power distribution has a half-normal peak due to the quasi-stationary detector noise and a long tail of the high SNR pixels due to the noise transients. The cross-power statistic has a much shorter tail because it helps to suppress the noise transients, which, in general, are not coherent between the detectors. For comparison, Figure 5 also shows the excess-power statistic corresponding to the geometric mean power estimator. It has more pixels in the high SNR tail due to the power leakage in the vicinity of the noise transients.

Figure 6 shows the wavescan excess-power and cross-power spectrograms for the binary neutron star merger GW170817 detected by LIGO and Virgo in 2017 [30, 31]. The GW170817 detection was obstructed by a loud glitch in the Livingston detector coincident with the event. The glitch can be seen in the excess-power spectrogram with its power well localized by the wavescan transform. In the cross-power spectrogram, the glitch is suppressed and does not obstruct the identification and reconstruction of the event.

By selecting the excess-power and the cross-power pixels in combination with an appropriate clustering method, a coherent transient event can be identified in the wavescan time-frequency data. The corresponding wavescan amplitudes can be used for the further analysis. The detector responses to a GW signal can be extracted from the noise using the maximum likelihood method [14]. All this analysis is outside of the scope of this paper. But to complete the wavescan transform, the next section describes the reconstruction of the time domain signals from the wavescan data.

IV. WAVESCAN EXPANSION

For a general windowed STFT the inverse transform can be defined as

$$x(t) = \sum_{n,m} g_{nm} w_s(t - t_n) e^{i\omega_m t}, \quad (19)$$

where $w_s(t)$ is the synthesis window, and g_{nm} are the expansion coefficients calculated for each time-frequency location enumerated by n and m . For a special case of the Gabor expansion, when $w_s(t)$ is a Gaussian window, the coefficients g_{nm} can be calculated by using Equation 1 with a specific analysis window $w_a(t)$ [32–34]. For the critical sampling $\Delta t \Delta \omega = 1$, the unique window $w_a(t)$ can be calculated such that g_{nm} are given by Equation 1. In general, for an oversampled Gabor transform with $\Delta t \Delta \omega < 1$, the analysis window is no longer unique [32]. Several methods had been suggested to calculate the analysis window function [32–34], which can be used to obtain the expansion coefficients g_{nm} . However, all these methods are not applicable for the wavescan transform where the analysis window is defined a priori and the wavescan amplitudes are obtained with windows of different duration. Therefore, we will search for an approximate solution for the expansion coefficients assuming that $w_a(t) = w_s(t)$, which is expected for the highly oversampled STFT [33].

It is convenient to introduce the wavescan wavelet in the stack that represents the local components of $x(t)$ at the time n , frequency m and different resolutions l

$$\chi_{lnm}(t) = \frac{1}{\sqrt{2}} \left[X_{lnm} \psi_{lnm}(t) + \tilde{X}_{lnm} \tilde{\psi}_{lnm}(t) \right]. \quad (20)$$

Since only one wavelet is selected from each stack, l is the internal wavescan parameter and omitted below. The expansion of the time series $x(t)$ can be approximated as a superposition of the selected wavescan wavelets $\chi_{nm}(t)$

$$x'(t) = \sum_{n,m} \alpha_{nm} \chi_{nm}(t), \quad (21)$$

where the α_{nm} are unknown expansion coefficients. This expansion is not conceptually different from Equation 19. For a single resolution Gabor transform described in [32–34], the coefficients α_{nm} are not explicitly calculated, but they are implicitly defined by the calculation of the analysis window. Since this is not possible for the wavescan transform, a different approach is used for the calculation of α_{nm} .

As one may expect, for a highly oversampled transform at zero order approximation the coefficients α_{nm} should be equal to the oversampling factor

$$\alpha_{nm}^0 = \Delta t \Delta \omega. \quad (22)$$

For a single resolution STFT with sufficient oversampling, the coefficients α_{nm}^0 provide a quite accurate approximation for $x(t)$ with a typical residual amplitude

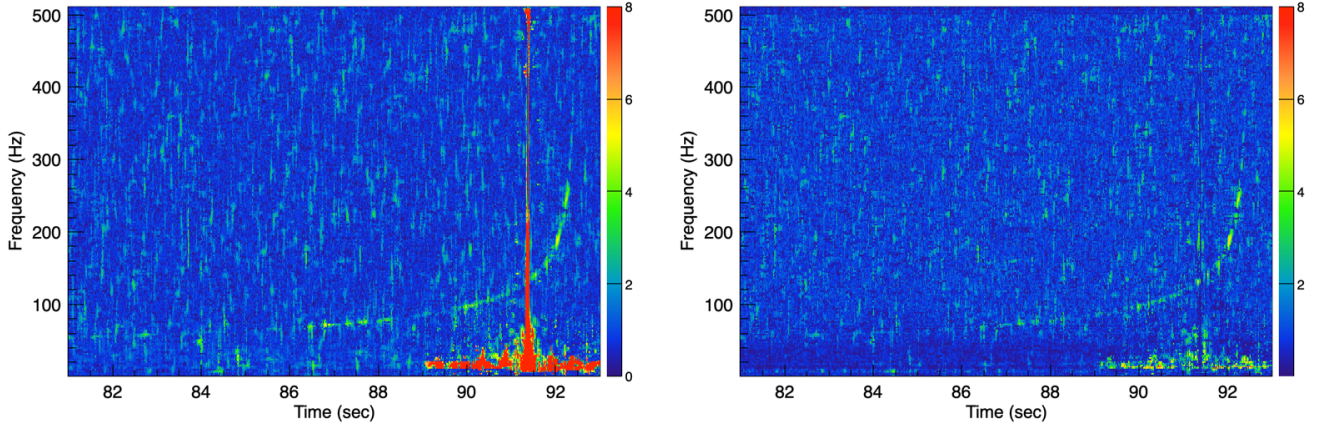


FIG. 6. HL-network time-frequency distributions at the time of the GW170817 event: left - excess power, right - cross power.

error $|x(t) - x'(t)|$ of a few percents. For example, a consecutive forward and inverse transforms of a white Gaussian noise with the window width of $T_w = 1/8$ s and two different sampling factors $\Delta t \Delta \omega = \{1/64, 1/32\}$ have the residual errors that follow the Gaussian distribution with the standard deviation σ_0 of a few percent (see Table I). The frequency analysis of the residual data (Figure 7, black curve) shows that these errors are due to the boundary artifacts, and for signals, well inside the data frequency band, the reconstruction errors are below 10^{-5} . The same expansion for the wavescan data produces significantly larger errors ($\sim 25\%$) that are uniform across the frequency band. To explain these results,

$\Delta t \Delta \omega$	STFT			wavescan		
	σ_0	σ_1	σ_2	σ_0	σ_1	σ_2
1/32	4.4%	1.3%	0.7%	26%	7.3%	4.1%
1/64	2.1%	0.5%	0.2%	25%	6.1%	3.1%

TABLE I. Accuracy of the forward-inverse transform for the single-resolution STFT and the multiresolution wavescan transform ($L = 6$), for the first three approximations of the expansion coefficients.

we should recall that unlike for an orthogonal transform, Equation 21 is a sum of strongly correlating wavelets. For the single-resolution STFT they are compensating each other resulting in the accurate reconstruction. On the contrary, the wavescan wavelets are selected from the multiresolution wavelet set. The selected wavelets lose their correlating partners and, hence, the reconstruction accuracy. Therefore, we should expect a similar loss of accuracy for the single-resolution STFT used in any practical analysis that requires modifications of the wavelet data. For example, by selecting the excess-power wavelets for transient events, we should expect much larger reconstruction errors for the inverse Gabor transform [32–34] compared to its accuracy estimated with the forward-inverse test. For wavelets that are close

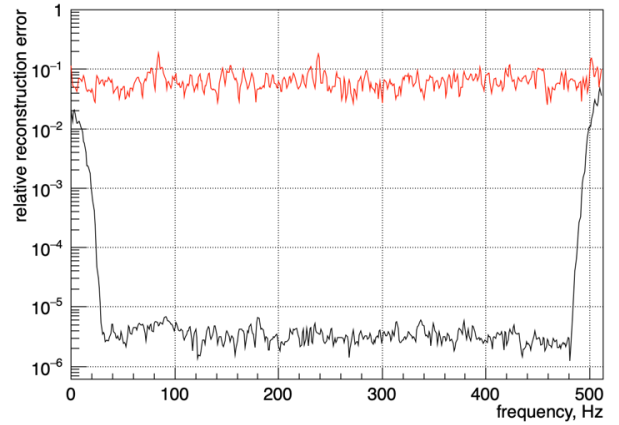


FIG. 7. Reconstruction errors vs frequency for the forward-inverse transform of the white Gaussian noise. Black - single-resolution STFT ($T_w = 1/8$ s, $\Delta t \Delta \omega = 1/64$). The overall reconstruction error is 0.7%. The reconstruction accuracy is significantly better in the center of the frequency band. Red - the reconstruction error of the inverse wavescan transform with $L=8$ resolutions. The residual error is around 8% and is uniform across the frequency band. In both cases the α_{nm}^1 expansion coefficients are used.

to the boundaries of the selected time-frequency area, the expansion coefficients are no longer optimal because they are not accounting for the missing wavelets. Therefore, the expansion coefficients should be re-calculated every time when the wavelet data is modified by the filtering algorithms.

The zero-order approximation errors $\sigma_0 \approx 25\%$ are too large for the wavescan transform where the window resolution varies from pixel to pixel. It requires a more accurate approximation for α_{nm} which can be found from the minimization of the residual error $|x(t) - x'(t, \alpha_{nm})|^2$. The resulting system of linear equations for α_{nm} is hard

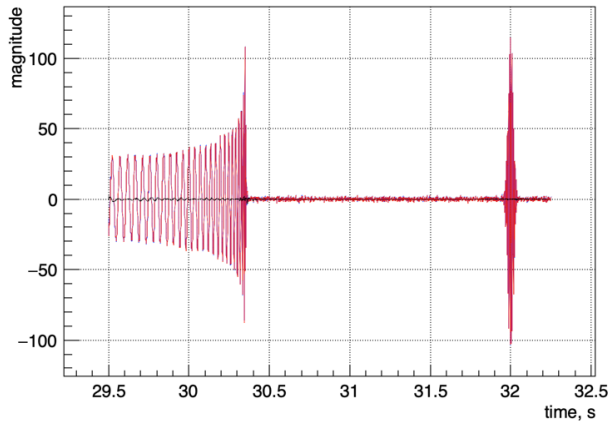


FIG. 8. Reconstruction of the test BBH and cos-Gaussian signals embedded into the white Gaussian noise with the unity variance: red - reconstructed $x'(t)$, blue - original $x(t)$ (barely visible behind red), black - residual $x(t) - x'(t)$. For the first order α_{nm}^1 expansion coefficients, the reconstruction error is $\sim 4\%$ for the segment of data with the noise only, and it is close to a percent for the deterministic signals.

to solve and, moreover, it does not have a unique solution

$$\sum_{\mu\nu} \alpha_{\mu\nu} \langle \chi_{nm}, \chi_{\mu\nu} \rangle = \langle \chi_{nm}, \chi_{nm} \rangle. \quad (23)$$

But it inspires an iteration procedure converging to a small residual error. The iteration is based on the calculation of the cross-talk integrals $\langle \chi_{nm}, \chi_{\mu\nu} \rangle$ between the wavelet χ_{nm} and the nearby wavelets. The cross-talk integrals can be evaluated by using the known overlap between the corresponding STFT wavelets. The higher order approximations for α_{nm}^i are obtained by iterations starting with the zero-order expansion coefficients ($i = 0$)

$$\alpha_{nm}^{i+1} = \frac{\alpha_{nm}^i \langle \chi_{nm}, \chi_{nm} \rangle}{\sum_{\mu\nu} \alpha_{\mu\nu}^i \langle \chi_{nm}, \chi_{\mu\nu} \rangle}, \quad (24)$$

where the summation is performed over all nearby pixels that have a non-zero overlap with the pixel nm . The iteration procedure is regularized by limiting the value of the expansion coefficients in the range $0 < \alpha_{nm} < 1$.

As shown in Table I, for the Gaussian noise test with the single-resolution STFT and the two different oversampling factors, the first (σ_1) and the second (σ_2) order approximations significantly reduce the boundary artifacts reaching the accuracy below 1%, and preserve the accurate reconstruction of signals that are away from the boundaries. This simple and surprisingly accurate approximation of the inverse STFT is sufficient for most signal processing applications that are using a single resolution STFT regression. The next order approximations provide a reasonable reconstruction accuracy for the inverse wavescan transform as well. Depending on the wavescan transform parameters, the residual amplitude errors increase with the number of resolutions L and

for $L=8$ they are approximately 8% for the first-order approximation. Respectively, by using the second-order approximation, the reconstruction errors can be reduced down to a few percent. The reconstruction errors are better for the deterministic signals, approaching the reconstruction accuracy of a percent as shown in Figure 8. While a more accurate inverse wavescan transform can be obtained, the first and the second order approximations are usually sufficient for the reconstruction of the time-domain GW signals, which is dominated by the errors due to the detector noise.

V. CONCLUSION

This paper presents the multiresolution regression of gravitational wave data, including the estimation of the time-dependent signal power, extraction of signals from noise in the wavelet domain, and reconstruction of their time-domain waveforms. It describes the wavescan transform, which scans the local spectral power with the multiresolution STFT wavelets, and produces a time-frequency distribution where the temporal and spectral leakage artifacts are suppressed by selecting wavelets with the optimal resolution. The wavescan spectrograms provide a high-resolution visualization of the time-dependent signal components. Two novel statistics based on the excess-power and cross-power of multiple detector channels enable an efficient identification of transient signals in the data. A simple and accurate approximation for the inverse STFT is introduced. The inverse transform does not rely on a specific choice of the window function and can be used for any STFT with sufficient oversampling. The accuracy of the inverse STFT should be adequate for most signal processing applications that are using a single resolution STFT. The inverse wavescan transform is less accurate. However, it can be used for the reconstruction of the time-domain GW signals with the accuracy of a few percent. While the wavescan regression is developed primarily for the analysis of the gravitational wave signals, it can be also used for the analysis of any non-stationary time series.

VI. ACKNOWLEDGMENTS

The author thanks G. Vedovato for useful discussion and comments on the paper. This research has made use of data, software, and/or web tools obtained from the Gravitational Wave Open Science Center, a service of LIGO Laboratory, the LIGO Scientific Collaboration, and the Virgo Collaboration. This research was supported by the US National Science Foundation grants PHY-0244902 to the University of Florida, Gainesville, Florida.

-
- [1] J. W. Cooley and J. W. Tukey, *Math. Comput.* **19**, 297 (1965).
 - [2] D. Gabor, *Journal of the IEE* **93**, 429 (1946).
 - [3] B. P. Abbott *et al.* (LIGO Scientific Collaboration and Virgo Collaboration), *Phys. Rev. Lett.* **116**, 241102 (2016).
 - [4] S. Mallat, *A Wavelet Tour of Signal Processing, Third Edition: The Sparse Way*, 3rd ed. (Academic Press, Inc., USA, 2008).
 - [5] S. Chatterji, L. Blackburn, G. Martin, and E. Katsavounidis, *Classical and Quantum Gravity* **21**, S1809–S1818 (2004).
 - [6] F. Robinet, N. Arnaud, N. Leroy, A. Lundgren, D. Macleod, and J. McIver, *SoftwareX* **12**, 100620 (2020).
 - [7] L. Cohen, *Proceedings of the IEEE* **77**, 941 (1989).
 - [8] P. Wigner, *Phys. Rev. D* **40**, 749 (1932).
 - [9] J. Ville, *Cables et Transmission* **2A**, 61 (1948).
 - [10] L. Cohen, *Journal of Mathematical Physics* **7**, 781 (1966), <https://doi.org/10.1063/1.1931206>.
 - [11] P. Loughlin, J. Pitton, and B. Hannaford, *IEEE Signal Processing Letters* **1**, 199 (1994).
 - [12] J. Nam, G. J. Mysore, J. Ganseman, K. Lee, and J. S. Abel, in *INTERSPEECH* (Makuhari, Japan, 2010) pp. 1696–1699.
 - [13] V. V. Moca, H. Bârzan, A. Nagy-Dabacan, and R. C. Mureşan, *Nature Communications* **12**, 18 (2021).
 - [14] S. Klimenko, G. Vedovato, M. Drago, F. Salemi, V. Tiwari, G. A. Prodi, C. Lazzaro, K. Ackley, S. Tiwari, C. F. Da Silva, and G. Mitselmakher, *Phys. Rev. D* **93**, 042004 (2016).
 - [15] S. Klimenko, I. Yakushin, A. Mercer, and G. Mitselmakher, *Classical and Quantum Gravity* **25**, 114029 (2008).
 - [16] S. Klimenko, S. Mohanty, M. Rakhmanov, and G. Mitselmakher, *Phys. Rev. D* **72**, 122002 (2005).
 - [17] S. Klimenko, G. Vedovato, *et al.*, “Coherent waveburst,” (2020), <https://www.gwburst.gitlab.io/>, [gwburst.gitlab.io/](https://www.gwburst.gitlab.io/).
 - [18] V. Necula, S. Klimenko, and G. Mitselmakher, *Journal of Physics, Conference Series* **363**, 012032 (2012).
 - [19] B. P. Abbott *et al.* (LIGO Scientific Collaboration and Virgo Collaboration), *Phys. Rev. Lett.* **116**, 061102 (2016).
 - [20] B. P. Abbott *et al.* (LIGO Scientific Collaboration and Virgo Collaboration), *Phys. Rev. X* **9**, 031040 (2019).
 - [21] R. Abbott *et al.* (LIGO Scientific Collaboration and Virgo Collaboration), *Phys. Rev. X* **11**, 021053 (2021).
 - [22] T. L. S. Collaboration, the Virgo Collaboration, and the KAGRA Collaboration, “Gwtc-3: Compact binary coalescences observed by ligo and virgo during the second part of the third observing run,” (2021), [arXiv:2111.03606 \[gr-qc\]](https://arxiv.org/abs/2111.03606).
 - [23] J. Aasi *et al.* (LIGO Scientific Collaboration), *Classical and Quantum Gravity* **32**, 074001 (2015).
 - [24] F. Acernese *et al.* (Virgo Collaboration), *Classical and Quantum Gravity* **32**, 024001 (2014).
 - [25] S. Cheung and J. Lim, *IEEE Transactions on Signal Processing* **40**, 975 (1992).
 - [26] V. Tiwari, M. Drago, V. Frolov, S. Klimenko, G. Mitselmakher, V. Necula, G. Prodi, V. Re, F. Salemi, G. Vedovato, and I. Yakushin, *Classical and Quantum Gravity* **32**, 165014 (2015).
 - [27] B. P. Abbott *et al.* (LIGO Scientific Collaboration and Virgo Collaboration), *Classical and Quantum Gravity* **33**, 134001 (2016).
 - [28] S. C. Choi and R. Wette, *Technometrics* **11**, 683 (1969).
 - [29] D. Davis, J. S. Areeda, B. K. Berger, R. Bruntz, A. Effler, R. C. Essick, R. P. Fisher, P. Godwin, E. Goetz, and A. F. Helmling-Cornell, *Classical and Quantum Gravity* (2021), [10.1088/1361-6382/abfd85](https://doi.org/10.1088/1361-6382/abfd85).
 - [30] B. P. a. Abbott (LIGO Scientific Collaboration and Virgo Collaboration), *Phys. Rev. Lett.* **119**, 161101 (2017).
 - [31] B. P. Abbott *et al.*, *The Astrophysical Journal Letters* **848**, L12 (2017).
 - [32] M. Bastiaans, *Proceedings of the IEEE* **68**, 538 (1980).
 - [33] J. Wexler and S. Raz, *Signal Processing* **21**, 207 (1990).
 - [34] S. Qian and D. Chen, *IEEE Transactions on Signal Processing* **41**, 2429 (1993).